remote sensing

MDPI

Article

Refined Coseismic Slip and Afterslip Distributions of the 2021 Mw 6.1 Yangbi Earthquake Based on GNSS and InSAR Observations

Zheng Liu, Keliang Zhang *, Weijun Gan and Shiming Liang

State Key Laboratory of Earthquake Dynamics, Institute of Geology, China Earthquake Administration, Beijing 100029, China; liuzheng22@mails.ucas.ac.cn (Z.L.); wjgan@ies.ac.cn (W.G.); liangshiming@ies.ac.cn (S.L.)
* Correspondence: klzhang@ies.ac.cn

Abstract: On 21 May 2021, an Mw 6.1 earthquake occurred in Yangbi County, Dali Bai Autonomous Prefecture, Yunnan Province, with the epicenter located in an unmapped blind fault approximately 7 km west of the Weixi-Qiaohou fault (WQF) on the southeastern margin of the Qinghai–Tibetan Plateau. While numerous studies have been conducted to map the coseismic slip distribution by using the Global Navigation Satellite System (GNSS), Interferometric Synthetic Aperture Radar (InSAR) and seismic data as well as their combinations, the understanding of deformation characteristics during the postseismic stage remains limited, mostly due to the long revisiting time interval and large uncertainty of most SAR satellites. In this study, we refined coseismic slip and afterslip distributions with nonlinear inversions for both fault geometry and relaxation time. First, we determined the fault geometry and coseismic slip distribution of this earthquake by joint inversion for coseismic offsets in the line-of-sight (LOS) direction of both Sentinel-1A/B ascending and descending track images and GNSS data. Then, the descending track time series of Sentinel-1 were further fitted using nonlinear least squares to extract the coseismic and postseismic deformations. Finally, we obtained the refined coseismic slip and afterslip distributions and investigated the spatiotemporal evolution of fault slip by comparing the afterslip with aftershocks. The refined coseismic moment magnitude, which was of Mw 6.05, was smaller than Mw 6.1 or larger, which was inferred from our joint inversion and previous studies, indicating a significant reduction in early postseismic deformation. In contrast, the afterslip following the mainshock lasted for about six months and was equivalent to a moment release of an Mw 5.8 earthquake. These findings not only offer a novel approach to extracting postseismic deformation from noisy InSAR time series but also provide valuable insights into fault slip mechanisms associated with the Yangbi earthquake, enhancing our understanding of seismic processes.

Keywords: InSAR; GNSS; Yangbi earthquake; SBAS; coseismic slip distribution inversion; afterslip fitting

check for updates

Citation: Liu, Z.; Zhang, K.; Gan, W.; Liang, S. Refined Coseismic Slip and Afterslip Distributions of the 2021 Mw 6.1 Yangbi Earthquake Based on GNSS and InSAR Observations. *Remote Sens.* **2024**, *16*, 3996. https://doi.org/10.3390/rs16213996

Academic Editor: Michele Saroli

Received: 30 August 2024
Revised: 17 October 2024
Accepted: 24 October 2024
Published: 28 October 2024

Copyright: © 2024 by the authors. Licensee MDPI, Basel, Switzerland. This article is an open access article distributed under the terms and conditions of the Creative Commons Attribution (CC BY) license (https://creativecommons.org/licenses/by/4.0/).

1. Introduction

On 21 May 2021, an Mw 6.1 earthquake occurred in Yangbi County, Dali Prefecture, Yunnan Province, China. According to the China Earthquake Networks Center, the earthquake struck at 21:48:34 local time (13:48:34 UTC), with the epicenter located at [99.87°E, 25.67°N]. The mainshock was preceded and followed by an intense earthquake sequence that had initiated three days prior to the mainshock, including an Ms5.6 foreshock that occurred approximately 27 min prior to the mainshock, and an Ms5.2 aftershock within 10 min after the mainshock, indicating a typical foreshock–mainshock–aftershock sequence [1–3]. Given such a unique seismic pattern, numerous studies based on geophysical observations have been conducted to reveal the complexities of this earthquake from different aspects, such as seismicity and seismogenic fault geometry [1,4–8], deep structure [9–11], and rupture directivity [12–14], highlighting our understanding of the tectonic background and

dynamic processes of this earthquake. Meanwhile, geodetic studies based on GNSS, InSAR as well as their combinations have revealed static coseismic slip distribution [3,15–20]. These studies have shown that the earthquake was primarily characterized by right lateral motion, accompanied by a minor normal fault component. Such a slip pattern is compatible with both the long-term tectonic stress and present-day strain rate of the region [14,21].

However, constrained from static coseismic deformation, one cannot detect the temporal process of afterslip, which is the ongoing deformation of coseismic slip. As an integral part of the total strain budget released during an earthquake sequence [22], afterslip may further enhance aftershocks through redistributing stress to its adjacent fault segments. Consequently, afterslip usually shares a similar pattern of temporal decay as aftershocks. In contrast to discontinuous aftershocks, afterslip reflects a gradual release of accumulated strain along the seismogenic fault. A general trend of postseismic deformation is to decay logarithmically with time after an earthquake [23], and the percentage of the released moment due to afterslip can be significant and even greater than the coseismic moment [24,25]. For example, after the 2004 Mw6.0 Parkfield, California, earthquake [26,27], the accumulated aseismic moment over five years was larger than that of its mainshock [24,25,28]. Therefore, quantifying the contribution of afterslip to the total strain release and understanding its interplay with aftershocks will provide important and detailed clues for comprehensive seismic hazard assessments and for developing models that can better predict the behavior of fault systems after an earthquake.

Recently, combined with GNSS and InSAR data, kinematic slip process models [14,29,30] have also revealed unilateral rupture propagation, initiating at the hypocenter and then expanding as a slip–pulse southward about 12 km along strike, temporally similar to the migration pattern of aftershocks. When such a rapid slip process stops, the seismogenic fault may be dominated by afterslip. As a result, both daily GPS solutions [15] and InSAR data, especially those several days after the mainshock, may contain a large amount of deformation during the postseismic stage [16,17,19]. In fact, Lu et al. [19] attempted to extract postseismic deformation with InSAR time series 6 months after the mainshock, and they estimated a peak cumulative postseismic deformation of 18 mm, with a peak rate about 3.5 cm/yr, in the southeast segment of the seismogenic fault. The descending postseismic deformation acquired from Sentinel-1 showed an uplift trend on the east of the seismogenic fault, similar to the coseismic deformation. If part of these postseismic deformations is misleadingly included in the estimate of coseismic displacements, the moment magnitude of the mainshock will be overestimated. To date, because of the 12-day revisiting time interval of Sentinel satellites and tropospheric stratification delays in this region [31], no studies have been conducted to specifically investigate postseismic surface deformation and fault afterslip, especially including the first week, using InSAR technology.

In this paper, we will first map coseismic slip distribution by conducting joint inversion from the GNSS data and both ascending and descending InSAR images, then refine the coseismic slip and afterslip after extracting both the coseismic offsets and postseismic deformation from the resampled InSAR time series with nonlinear least squares, and finally compare such refined coseismic inversion with the joint inversion and discuss the spatiotemporal interplay between the afterslip and aftershocks. Our results will provide a new method for extracting postseismic deformation from high-noise InSAR time series, and the refined coseismic slip distribution will contribute to a better understanding of the strain partitioning during different stages of the Yangbi earthquake.

2. Background of the Study Area

The 2021 Yangbi Mw 6.1 earthquake occurred on an unmapped fault located ~26 km from Dali City in southwestern China (Figure 1). The seismogenic fault was ~5 km west to the NW-trending Weixi-Qiaohou fault (WQF). Serving as geological boundary zones [32,33], both the WQF and the Red River Fault (RRF) exhibited dextral strike-slip characteristics and shared similar kinematic properties. Although there is ongoing debate about whether

the WQF is part of the RRF, these two faults together controlled the geological activity of the boundary zone, where regional seismicity was relatively high [34]. Geological investigations after the Yangbi earthquake indicated that there was no significant surface rupture, except for surface fractures about 5 km long [35]. The absence of surface rupture information further complicated the task of constraining the fault geometric parameters.

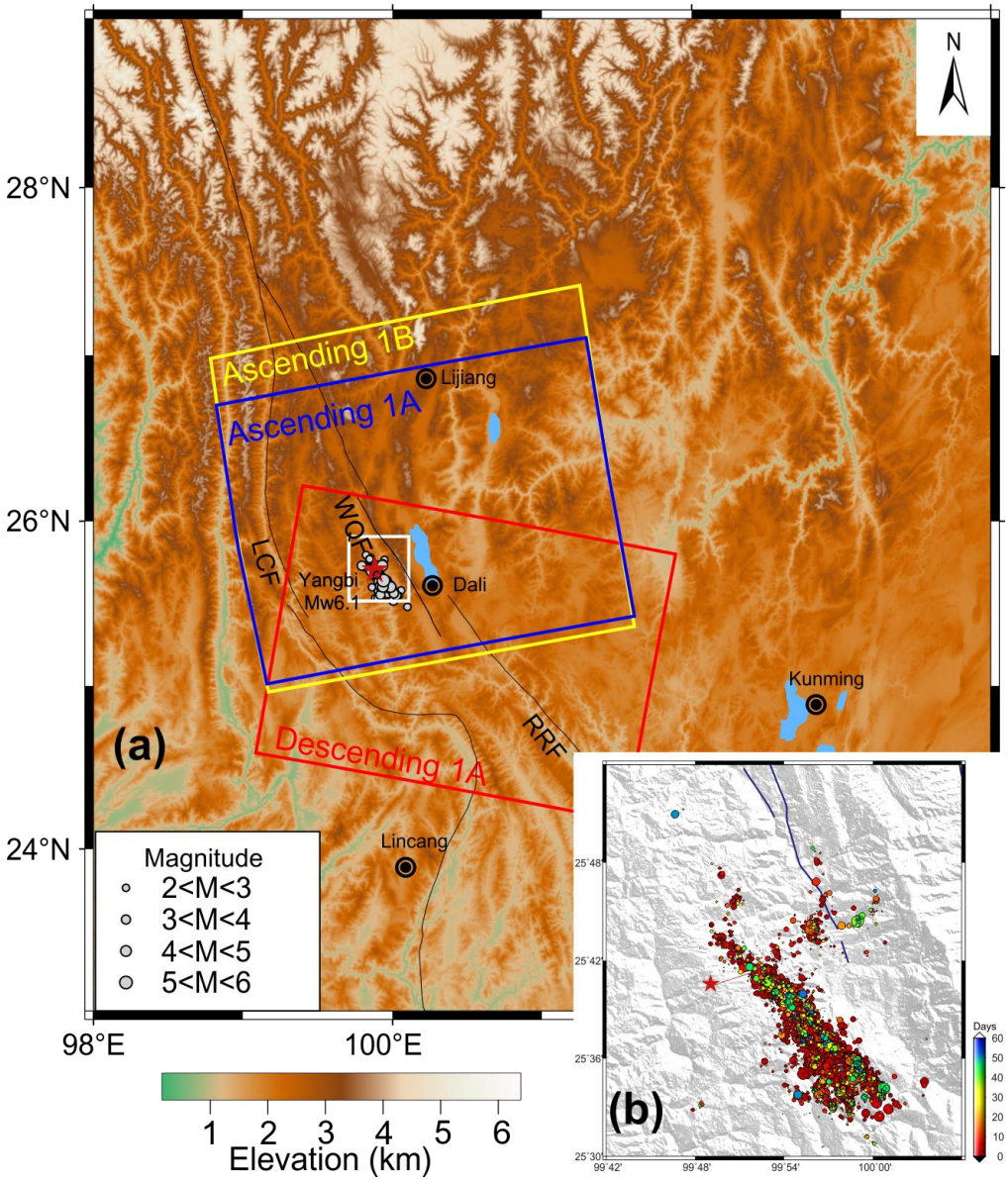


Figure 1. (**a**) Tectonics and SAR tracks of the Yangbi Region. The black lines indicate active faults near the epicenter. The image frames for Sentinel-1A ascending (blue box), Sentinel-1A descending (red box) and Sentinel-1B ascending (yellow box) are shown. The red star represents the epicenter of the 2021 Yangbi Mw6.1 earthquake. The white box indicates the position of (**b**). Aftershock data were provided by Tian et al. (2023) [21]. Abbreviations: WQF, Weixi-Qiaohou Fault; LCF, Lancangjiang Fault; RRF, Red River Fault. (**b**) Aftershocks in 60 days following the mainshock. The color bar depicts the days after the mainshock. Solid blue triangles denote GNSS stations.

The source mechanism for this earthquake was compiled by Harvard University's Global Centroid Moment Tensor (GCMT), the United States Geological Survey (USGS), the German Research Center for Geoscience (GFZ) and the China Earthquake Network Center (CENC) (Table 1). Although the epicenter was not well determined due to the lack of near-field seismic stations, all these focal mechanistic solutions showed a general

deformation in a right lateral strike-slip sense, with the hypocentral depth at 8–9 km and the centroid depths at 15–17.5 km, providing a depth constraint for both the fault geometry and coseismic slip distribution.

Table 1. Source parameters of the 21 May 2021 Yangbi earthquake given by different organizations.

Institution	Longitude/(°)	Latitude/(°)	Focal Depth/km	Plane I/(°)			Plane II/(°)			M_w
				Strike	Dip	Rake	Strike	Dip	Rake	
GCMT	100.02	25.61	15	315	86	168	46	78	4	6.1
USGS	100.01	25.76	17.5	135	82	–165	43	78	–9	6.1
CENC	99.87	25.67	8	–	–	–	–	–	–	6.4
GFZ	99.92	25.73	17	319	88	–165	–	–	–	6.0

3. Coseismic Deformation Field Derived from InSAR and GNSS

3.1. Data and Processing

The InSAR data used in this paper were downloaded from the NASA Alaska Satellite Facility (Alaska Satellite Facility). The data source included Sentinel-1A/B interferometric wide-swath mode SLC IW C-band imagery, with a VV polarization mode. Each image covered an area of 250 km × 250 km, with a resolution of 20 m × 5 m in the azimuth and range directions, respectively. The temporal baseline for the descending orbit images was 12 days (10 May 2021 to 22 May 2021), while for the ascending orbit images, it was 6 days (20 May 2021 to 26 May 2021). The spatial baselines were 48 m and 30 m, respectively. Shorter temporal and spatial baselines helped mitigate the effects of decorrelation on the deformation results.

The interferometric processing was implemented with the conventional two-pass differential InSAR strategy by the open-source software ISCE (v2.6.3) [36], which has been widely used in extracting ground deformation information from SAR images [37]. The 30 m resolution digital elevation data of the Space Shuttle Radar Topography Mission (SRTM) were used as auxiliary data to remove the influence of the topographic phase [38]. Multi-view processing was applied at a 5:1 ratio in both the range and azimuth directions, and precise orbital (AUX_POEORB) data from the European Space Agency (ESA) were used to eliminate orbital errors. To further improve the signal-to-noise ratio and minimize the effects of spatial and temporal baseline decoherence, the interferometric images were processed with an enhanced power spectral filtering method [39]. Additionally, the Generic Atmospheric Correction Online Service (GACOS) was used to remove tropospheric effects from each interferogram [40]. The GACOS data showed that the atmospheric errors in the ascending and descending track interferograms were obvious in this study area and appeared to be related to the topography. The ranges of atmospheric errors for the ascending and descending track interferograms were from −0.03 m to 0.01 m and from −0.01 m to 0.02 m, respectively [18,41]. Therefore, reducing the impact of atmospheric errors would significantly improve the accuracy of the derived ground displacements [18]. Additionally, in the southwestern region, where dense vegetation cover and heavy water vapor contributed to radar image decorrelation, this study increased the filtering window to 80 and enhanced the degree of filtering to improve the clarity of the interferometric fringes [40]. The generated phase interferogram was unwrapped using the minimum cost flow (MCF) algorithm [42] to obtain displacement data and the interferograms were geocoded into the WGS-1984 coordinate system to derive the coseismic deformation field of Yangbi. According to previous studies [3,35], some scholars utilized ascending track images (20 May 2021 to 1 June 2021) to obtain the coseismic deformation field of Yangbi, which may have been with the purpose of quickly retrieving the coseismic slip distribution. However, the presence of postseismic deformation within the first twelve days following the earthquake may have introduced more noise into their observations. Therefore, this study utilized the ascending track images from Sentinel-1B on 26 May 2021, five days after the mainshock, for a more accurate representation of the coseismic deformation field and

fault slip distribution. The detailed information about the ascending and descending tracks is listed in Table 2.

Table 2. InSAR ascending and descending track data parameters.

Orbit Direction	Imaging Date		Polarization	Azimuth Angle	Incident Angle	Spatial Baseline	Temporal Baseline
	Pre-Earthquake	Postseismic		α/(°)	θ/(°)	m	d
Ascending	20 May 2021	26 May 2021	VV	90	36.55	30	6
Descending	10 May 2021	22 May 2021	VV	90	42.16	48	12

Many researchers used only InSAR data [3,18,43] for fault inversion. However, the long temporal baseline of Sentinel-1A may have introduced a considerable amount of afterslip information, while data downsampling may have resulted in the loss of some information. These factors would have increased the uncertainty in estimating the fault slip. In comparison, near-field high-precision GNSS site displacement data could significantly improve the surface deformation accuracy affected by far-field noise, providing more detailed constraints on fault slip [44]. The joint inversion of the GNSS and InSAR data could enhance the reliability and stability of inversion [16]. Therefore, we incorporated data from four near-field GPS stations with significant displacements within 10 km on both sides of the fault [15] to constrain far-field deformation and refine the fault depth. The displacement information of the four near-field GPS stations is shown in Table 3.

Table 3. Four near-field GPS stations' data.

Serial Number	Station Name	Location		North–South Component (mm)	East–West Component (mm)	Vertical Component (mm)
		LON (°)	LAT (°)			
1	H204	99.92	25.72	−45.8	5.3	−2.1
2	YBZZ	99.79	25.66	1.3	−40.0	7.6
3	YBXL	99.91	25.64	33.0	−9.4	−44.2
4	YBZM	100.02	25.71	−14.2	26.9	−0.2

3.2. InSAR Coseismic Deformation

From the interferogram in Figure 2, it can be seen that the long axis of the main deformation field of the Yangbi earthquake was roughly oriented in the NW direction. The ascending track interferogram exhibited an elliptical pattern of fringes on the western side of the epicenter, while the descending track interferogram showed a symmetric butterfly-like distribution with more closely spaced interferometric fringes, located near the epicenter. The deformation field in the ascending orbit measured approximately 25 km in the north–south direction and 19 km in the east–west direction while in the descending orbit, it measured about 22 km in the north–south direction and 20 km in the east–west direction. The differences in flight attitude and satellite side view between the ascending and descending orbits resulted in different imaging patterns, leading to variations in the spatial distribution of the coseismic deformation. Figure 3a,b show the line-of-sight (LOS) deformation fields obtained from the Sentinel-1A/B ascending and descending orbit images. In these figures, positive (red) and negative (blue) deformation zones represent regions moving toward and away from the satellite, respectively. The ascending track interferogram indicated a line-of-sight (LOS) deformation ranging from −7 cm to 7 cm, while the descending track interferogram showed a range of −9 cm to 9 cm. The differing patterns observed in the interferograms (Figure 2) from the two tracks indicated that coseismic deformation was primarily characterized by horizontal rather than vertical movement, indicating a strong strike-slip component, as revealed by seismology-based focal mechanisms (see Table 1). What is more is that the absence of evident surface rupture in the field investigation suggests that this earthquake may have occurred on a blind fault [35].

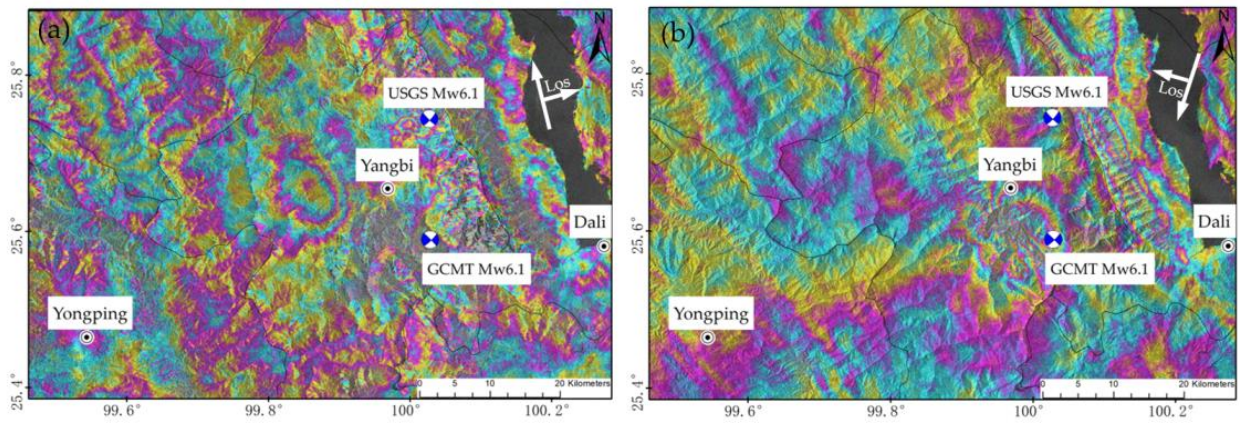


Figure 2. Interferograms of the 2021 Mw 6.1 Yangbi earthquake. The variation in fringe colors represents changes in LOS direction deformations: (**a**) on the ascending track between 20 May 2021 and 26 May 2021 and (**b**) on the descending track between 10 and 22 May 2021.

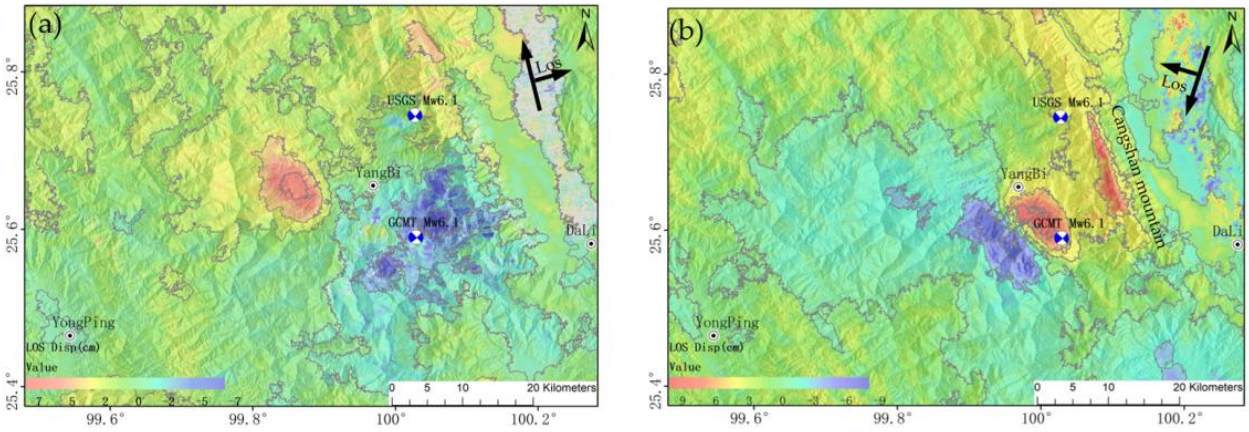


Figure 3. Line-of-sight (LOS) deformation maps of the 2021 Mw 6.1 Yangbi earthquake: (**a**) on the ascending track between 20 and 26 May 2021 and (**b**) on the descending track between 10 and 22 May 2021, red represents regions moving toward the satellite, while blue represents regions moving away from the satellite(with gray lines representing coseismic contours at 2 cm intervals).

4. Inversion of Fault Slip Distribution

4.1. Inversion of Fault Geometry

When all fault geometric parameters are known, surface displacement due to fault slip, d, can be expressed as a linear function between Green's function of fault geometric parameters and fault slip through Okada's finite fault dislocation model in an elastic half-space [45]:

$$d = G(X)\mathrm{s}(\delta) + \varepsilon \quad (1)$$

where $X = [L, W, x, y, D, \varphi, \theta]$ represents the fault geometric parameters (the fault length L, width W, depth D, the latitude and longitude for the starting point of the fault, the strike angle φ, and the dip angle θ), G represents Green's function corresponding to the unit slip of the fault plane, s is the uniform fault slip along the rake direction, δ is the rake angle and ε is the observation error.

In the first step, we determined fault geometric parameters by assuming a uniform slip on the fault plane through a nonlinear inversion. Such nonlinear inversion was conducted by prescribing bounded constraints on the fault geometric parameters with the Levenberg–Marquardt algorithm [46], which is primarily used for least squares curve fitting problems. This algorithm combines the steepest descent method and the Gauss–Newton method. It starts with an initial guess for the parameters and then iteratively updates these parameters

to minimize the sum of the squares of the residuals between the observations and the predictions:

$$\begin{gathered} \min : \sum (\mathrm{d} - \mathrm{G}(X) s(\delta))^2 \\ \text{subject to} : X_l \leq X \leq X_u \\ \delta_l \leq \delta \leq \delta_u \end{gathered} \tag{2}$$

where the initial values and the bounded values for the fault geometric parameter and rake angle were prescribed from the focal mechanism solution by the global CMT (GCMT, https://www.globalcmt.org, accessed on 25 July 2024). We set a smaller iterative range for these three parameters (the dip angle range was 80–90 degrees, the strike range was 130–150 degrees and the rake range was −210 to −150 degrees). The ranges for longitude and latitude were confined within a rectangular area that fully encompassed the deformation zone (99.832, 25.697; 100.115, 25.526), which was restricted from the relocated aftershocks by Yang et al. (2022). For the other four parameters, we set a broader iterative range: the length was limited to 9–20 km, the width to 2–15 km, the slip range to 0–1.5 m and the depth range to 0–5 km.

Moreover, the primary technical approach involved inversion on the constraints by the LOS deformation from ascending and descending tracks in the seismic area. Since data points obtained by InSAR are typically on the order of 10^8, the large amount of observations would have led to significant redundancy during the inversion. Such overabundance of observational data may sometimes be counterproductive, as it does not necessarily enhance detail but can instead introduce excessive noise into solutions. This additional noise can hinder the convergence of results, complicating the analytical process [47]. Therefore, in order to reduce the data volume and emphasize the main deformation information, we downsampled the InSAR data by dividing the main deformation area and the far-field deformation to achieve different levels of sampling density (Figure S1). In our experiments, we found that the resolution of the input data sampling and the presence of other deformation fields in the region significantly affected the depth and dip in the inversion results. Improving the sampling accuracy in the main deformation zone enhanced the coseismic signal, which could increase the earthquake magnitude and fault dip while shallowing the fault depth. However, excessively high sampling accuracy in the main deformation zone led to a large data volume and diminished the constraint effects of the far-field deformation on the fault parameters. After multiple comparisons, we found that a sampling frequency of 300 m in the mainshock center, combined with a 1000 m sampling frequency for far-field deformation signals, retained the spatial characteristics of the original deformation field and provided stable fault slip while ensuring accuracy. Additionally, we also found an abnormal uplift along Cangshan Mountain in the descending track images (Figure 3b). Since such abnormal signals associated with high relief are usually due to non-tectonic factors such as cloud and atmospheric delay [31], we masked this area prior to the inversion as other scholars have done [18].

Based on the interferometric fringe direction and deformation distribution from InSAR, we employed iterative processes by adjusting the parametric ranges to obtain the optimal solution. The algorithm was restarted multiple times to maximize the likelihood of the cost function converging to the global minimum. In the nonlinear inversion, a global minimum had to be tested at least three times to be deemed valid. The cost function tolerance was set to 0.001, with improvements below this threshold deemed negligible. Inversion was conducted with a maximum of 50 algorithmic restarts and 100 algorithmic iterations. A total of 15,212 ascending and 11,121 descending track data points were acquired, resulting in the identification of a NW–SE striking fault based on the deformation field.

For the near-field GPS data, we projected the 3D displacement of the GPS data to the LOS direction according to Equation (3) and set its weight ratio with the InSAR data to 10:1.

$$\begin{cases} \mathrm{d}_{LOS} = -d_e \cos(\alpha) \sin(\theta) + d_n \sin(\alpha) \sin(\theta) + d_u \cos(\theta) \\ {d_{Hor}}^2 = d_e^2 + d_n^2 \end{cases} \tag{3}$$

where d_{los} is the LOS deformation, α and θ are the azimuth and incidence angles of the radar satellite, respectively, and d_{Hor} is the horizontal displacement of the GPS site synthesized from the north–south(d_n) and east–west(d_e) displacements.

To assess the reliability of the fault geometric parameters, we used the Monte Carlo method to add noise perturbations to the inversion results, generating 100 sets of observations for reinversion. We also computed the posterior probability density functions (PDFs) of the inverted faults, which demonstrated that all fault geometric parameters were relatively stable. The optimal fault parameters are shown in Table 4.

Table 4. Optimal geometric parameters for fault constraints.

Parameters	Length (km)	Width (km)	Depth (km)	Dip (°)	Strike (°)	Lon (°)	Lat (°)	Slip (m)
Optimal	12.912	3.2554	0.954	82.75	139.67	99.92	25.644	0.8956
Mean	13.267	4.4436	0.340	80.69	141.14	99.919	25.641	0.8345
Standard deviation	1.636	1.9222	0.784	7.82	4.60	0.0077	0.0082	0.2472

Figure 4 shows the one-dimensional posterior distribution of the fault length, which reached the highest probability at 12.9 km, smaller than the ~20 km [21] that was delineated from aftershocks. The fault strike was 139° with a dip of 82.7° to the southwest, which was nearly identical to the focal mechanism from GCMT.

Additionally, we estimated a magnitude of Mw6.1, which was consistent with the results from both the USGS and GCMT. Figure 5 shows the final optimal solution of 100 iterations. From such an optimal model, the slip distribution depicted a clear right lateral strike-slip fault with a high dip angle, consistent with the seismic mechanism solutions from Feng et al. [48] and Yang et al. [49]. Located between the central regions of the two deformation zones, the rupture did not reach the surface and was thus consistent with a blind fault zone inclined to the southwest [15–17]. The optimal fault geometric parameters are shown in Table 5.

Table 5. Fault geometric characteristics of the mainshock area from the joint inversion of ascending and descending track images.

Type	Fault Length/m	Fault Width/m	Fault Depth/m	Dip	Strike
Asc–Des	12,912	3255	954.400	82.75	139
Type	**Epicentral Longitude**	**Epicentral Latitude**	**Rake**	**Slip/m**	**Mw**
Asc–Des	99.92	25.64	−171	0.80	6.1

Figures 6 and 7 show the InSAR coseismic deformation (Figures 6a and 7a), the predicted deformation based on the optimal fault model (Figures 6b and 7b) and the residuals (Figures 6c and 7c). The inversion results closely reproduced the coseismic deformation field. The residuals for both ascending and descending images were controlled to within 10 mm, with only sporadic errors up to 20 mm in the main deformation zone of the descending image, indicating that our model effectively simulated the coseismic deformation field of Yangbi. It is notable that the uniform fault slip model may not have captured the far-field deformation well, leading to perceptible residuals. Nevertheless, these residuals fell within an acceptable range of noise uncertainty, ensuring the overall reliability of our analysis. In addition, the ascending track data (20 May 2021 to 26 May 2021), acquired 6 days after the earthquake, showed significant residuals in some local areas near the fault (Figure 7c). One possible reason is that postseismic deformation occurred after the mainshock. Analysis of GPS displacement simulations showed that sites YBZZ and YBZM moved westward and eastward, respectively, while H204 and YBXL moved nearly north–south, confirming the dextral slip along the NW direction of the coseismic fault. The GNSS displacements indicated that the simulation results were very close to

the actual observations. These results demonstrated that the measured displacement data were effectively validated by the optimal fault simulation. Overall, the ascending and descending track simulations accurately reproduced the coseismic deformation field within an acceptable error range.

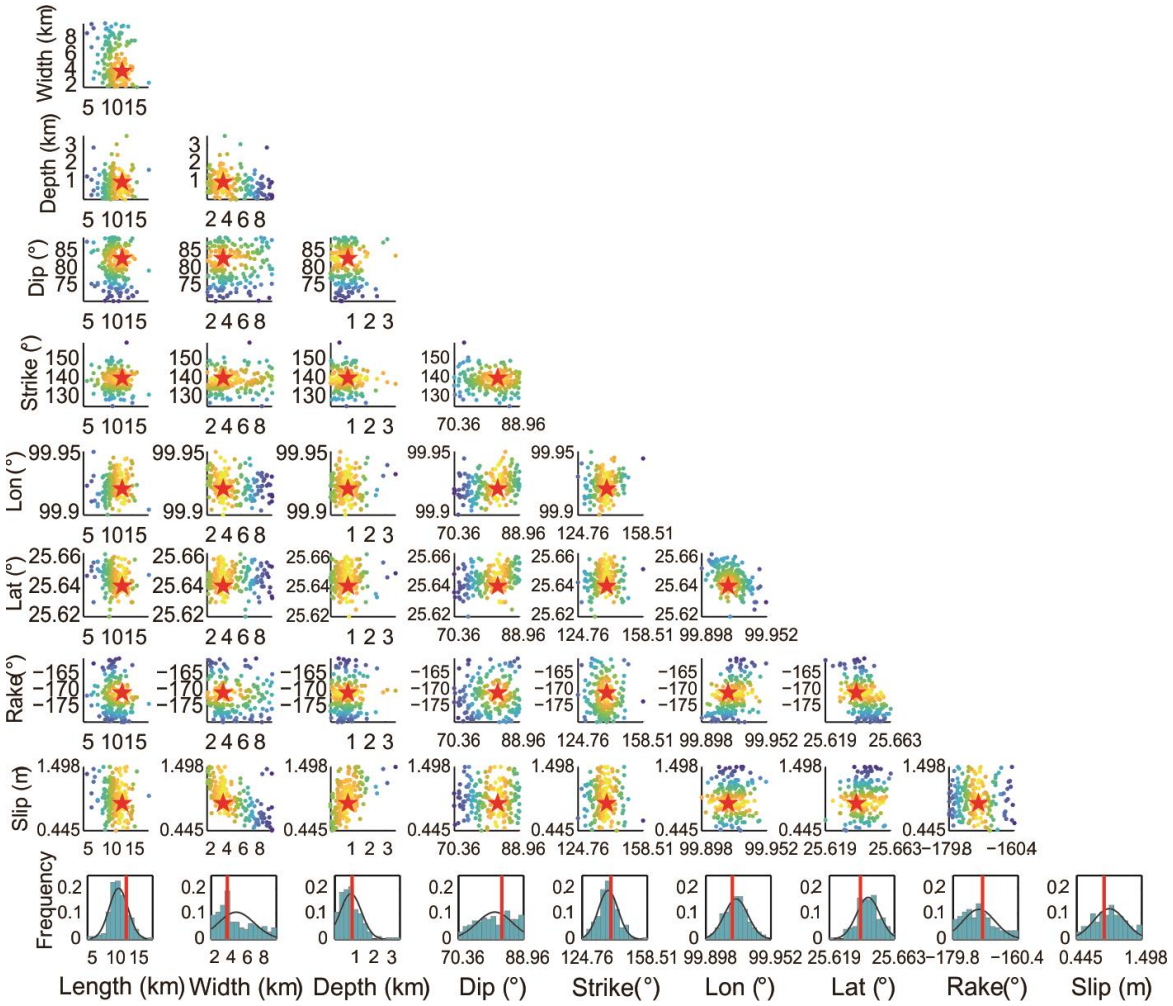


Figure 4. The posterior probability density distribution of the margins of the 2021 Yangbi earthquake fault. The bottom row shows the histograms of the marginal probability density distributions for each parameter. The black waved lines represent probability distribution curves and the red line represents the maximum a posteriori probability solution.

4.2. Inversion of Coseismic Fault Slip Distribution

In the second step, we inverted the slip distribution on our determined seismogenic fault plane in a linear squares sense. After dividing the fault plane into subfaults of specific sizes, we modeled the ground deformation field with the Okada elastic half-space dislocation and applied regularization with a second-order Laplacian smoothing constraint order to prevent divergence in the slip distribution solution. The equation to be solved was the following:

$$\begin{bmatrix} \mathrm{d}_{InSAR} \\ 0 \end{bmatrix} = \begin{bmatrix} G \\ \kappa\nabla^2 \end{bmatrix} \mathrm{s} + \begin{bmatrix} \varepsilon \\ 0 \end{bmatrix} \tag{4}$$

where d_{InSAR} is the observed surface deformation, G is Green's matrix, κ is the smoothing factor, ∇^2 is the Laplacian smoothing operator, s is the distributed slip vector and ε is the observation error.

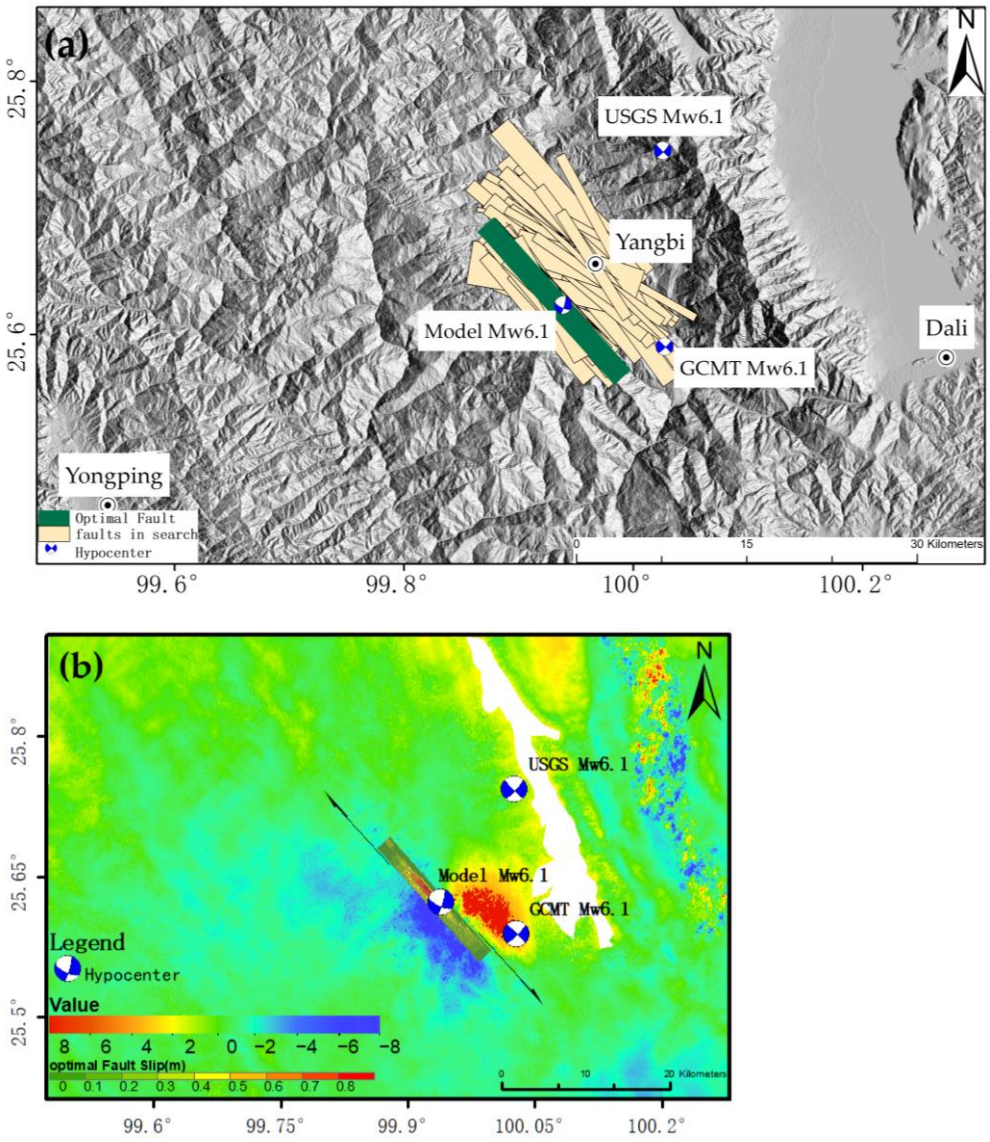


Figure 5. (**a**) Selected iterative search results of the fault geometry. The rectangles in beige denote faults during the search process and the rectangle in green represents the optimal fault geometry. (**b**) Spatial distribution characteristics of the optimal fault.

Based on previous studies of the historical data of the Yangbi earthquake and recent strong earthquakes in the central part of the WQF [50], combined with the spatial slip distribution characteristics of the fault, we set the initial slip surface of the Yangbi earthquake fault as 20 km long along the strike and 15 km wide along the dip with 1 km × 1 km slip patches. We had sufficient sampling density data to support precise slip on the fault surface, which was much more accurate than the 2 km × 2 km slip patch results of Liu et al. [30] and Zhang et al. [3]. For each slip patch, a fluctuation range of ±45° in its main slip direction was set to better adapt to the actual deformation field. To find an optimal coseismic slip inversion, we tested 100 smoothing factors (from 0.01 to 1). A higher smoothing factor makes the fault slip too smooth, while a lower smoothing factor causes severe mismatches in the slip results. Therefore, we determined 0.05 as the optimal smoothing factor value, balancing the root mean square (RMS) mismatch and model roughness. The inverted coseismic slip was located to the southeast side of the epicenter, primarily concentrated at depths between 4 and 10 km, with the peak slip of 0.7 m occurring at a depth of 6.9 km. The main slip zone (>0.5 m) extended approximately 6 km in length and 4 km in width, with a roughly rectangular shape that gradually weakened outward. Slip decreased rapidly

below 8 km, nearly ceasing around 10 km. The entire slip area was elongated, exhibiting clear right lateral strike-slip characteristics.

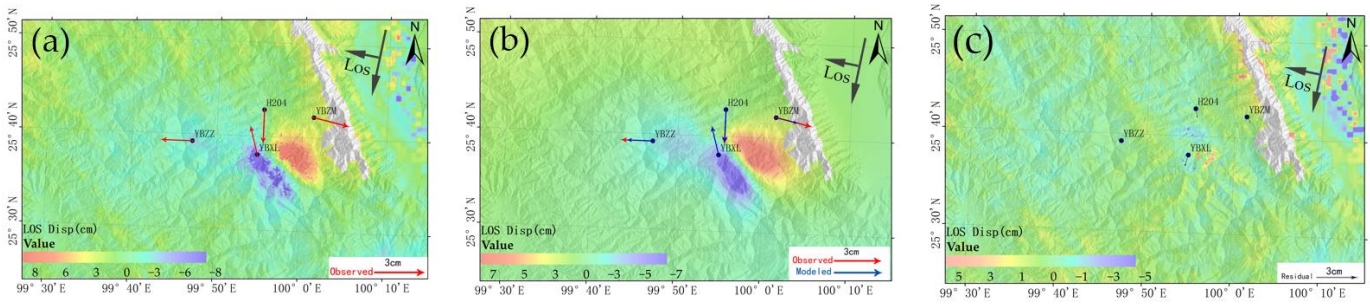


Figure 6. Coseismic deformation field model and inversion residuals: (**a**) coseismic deformation; (**b**) modeled result; and (**c**) residuals. The arrows represent the horizontal displacements of the GNSS stations, with red representing observed values, blue representing model values and black representing residuals (descending images from 10 to 22 May 2021).

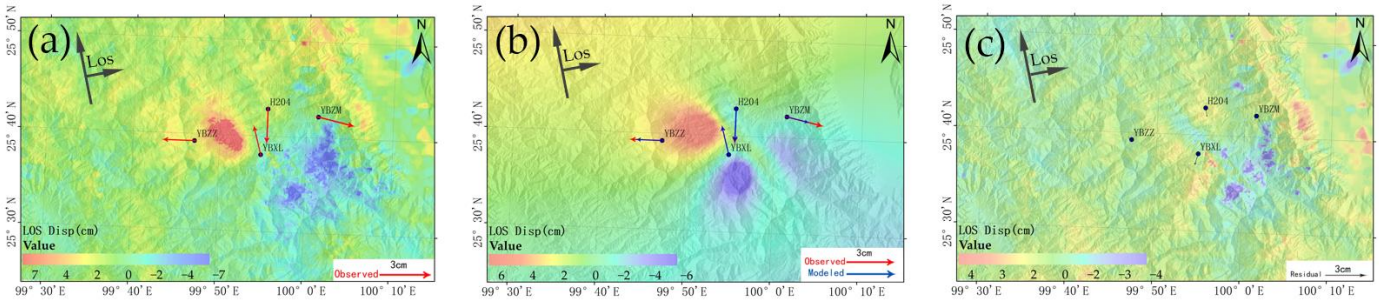


Figure 7. Coseismic deformation field model and inversion residuals: (**a**) coseismic deformation; (**b**) modeled result; and (**c**) residuals. The arrows represent the horizontal displacements of the GNSS stations, with red representing observed values, blue representing model values and black representing residuals (ascending images from 20 to 26 May 2021).

From the distribution of aftershocks, a total of 78 aftershocks of Ms2.9 or higher occurred within a week after the mainshock and were linearly arranged in a northwest–southeast direction, and the distribution of aftershocks corresponded to the unidirectional rupture of the northeast-trending fault from northwest to southeast. The Coulomb stress in the shallow part of this rupture continues to accumulate [18], so there is still some seismic risk in the future.

Our coseismic slip distribution model (Figure 8) indicated a significant right lateral strike-slip component for the Yangbi earthquake. The moment magnitude and slip amplitude derived from the integration of multiple geodetic datasets and the reduced interval between interferometric images showed slight discrepancies compared to some previous studies. In Section 5, we will further re-estimate the coseismic displacement by fitting postseismic time series derived from InSAR images, aiming to obtain a more detailed pattern of the fault slip.

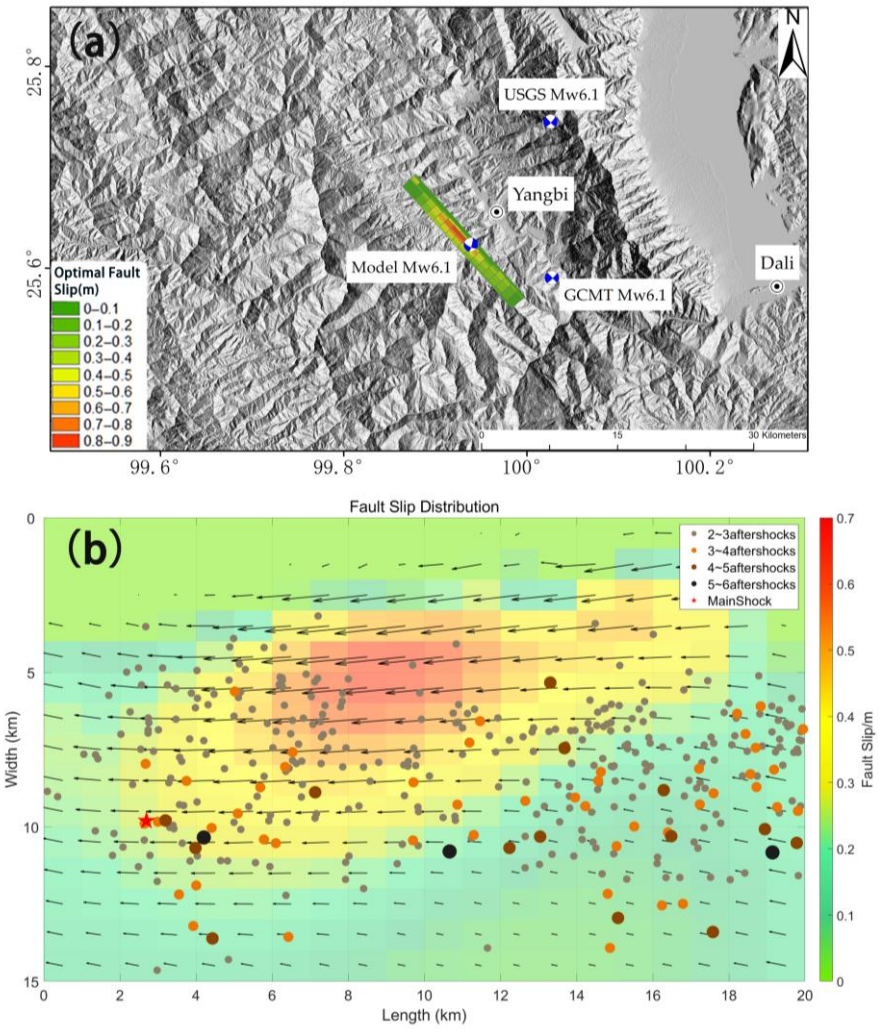


Figure 8. (**a**) Spatial distribution of coseismic fault slip for the optimal solution. (**b**) Coseismic slip distribution on the fault plane. The black arrows represent the direction of slip of the subfaults. The aftershocks were provided by Tian et al. [21].

5. Refined Coseismic Slip and Afterslip

The 2021 Yangbi Mw 6.1 earthquake occurred in an area that was significantly impacted from non-tectonic factors such as atmospheric conditions and cloud cover [31]. These non-tectonic factors resulted in severe decoherence between the SAR images acquired at different times during the postseismic stage. To date, no studies have been conducted to specifically investigate postseismic surface deformation and fault afterslip in the Yangbi area using InSAR technology.

In this section, we re-estimated coseismic offsets and extracted postseismic displacements from InSAR time series with nonlinear least squares fitting and then mapped both coseismic slip and afterslip distributions. This approach was expected to enhance our understanding of the true subsurface slip distribution along the causative faults in Yangbi and refine our interpretation of the fault rupture process.

5.1. Time-Series Data Preparation and Processing

Compared to the ascending track images, the descending track images displayed a more concentrated deformation zone. At the same time, their time-series atmospheric data were relatively stable. Therefore, we selected 22 descending images from a ten-month period, spanning from 10 May 2021 to 6 March 2022, for processing. The time-series data were processed using the small baseline subset (SBAS) module of Mintpy [51], which

improves data coherence by setting the azimuthal multi-look to 5 and the range multi-look to 20. Precision orbit information was incorporated to correct systematic errors, and GACOS [40,52] was used to remove tropospheric effects. For time-series processing, the image on 22 May 2021, the first day after the earthquake, was chosen as the reference image. In order to facilitate image unwrapping and region selection, we set the minimum coherence for the interferometric network and postseismic time series to be 0.5 and for reference points to 0.6.

Figure 9 shows that the postseismic surface deformation was predominantly focused in the same deforming areas of the mainshock. It initially amounted to only 4 cm, starting from 3 June 2021, and became most pronounced on 25 October 2021, reaching a peak of 9 cm. Following this peak, the increased rate of deformation decelerated, and the cumulative amount of deformation began to gradually level off. It is notable that the October 25 image clearly delineated two separate zones, which could have been due to the favorable atmospheric conditions during image capture.

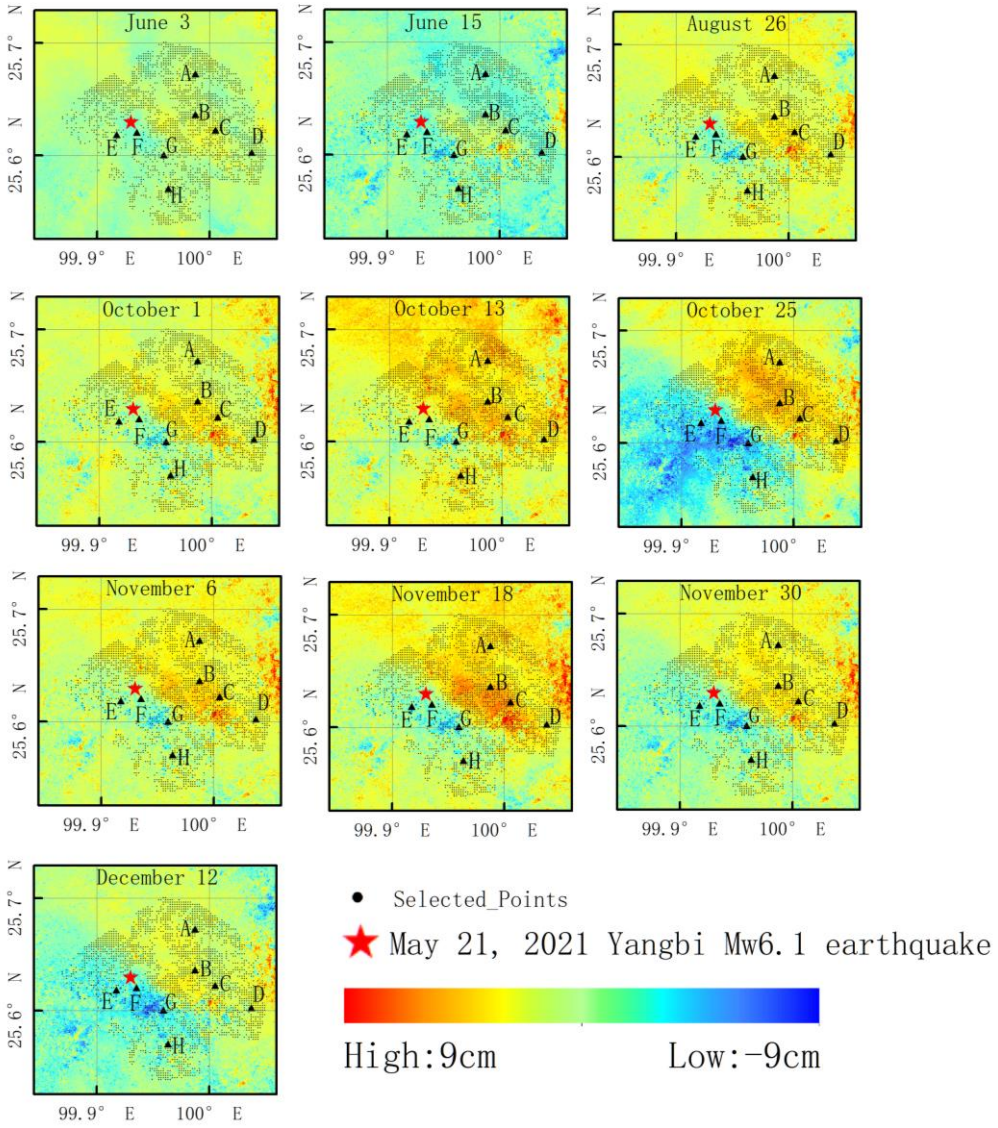


Figure 9. Temporal characteristics of the surface deformation in 6 months after the mainshock of the Yangbi earthquake. The red star denotes the epicenter of the mainshock. Black dots (Selected_Points) denote 2191 points used to refine the coseismic offset and extract postseismic deformation. The black triangles represent eight points (A–H) from the "black dots" and their time series are displayed in Figure 9.

5.2. Re-Estimate of Coseismic Offsets and Extraction of Postseismic Deformation

The postseismic deformation field was primarily a response to afterslip, poroelastic rebound and viscoelastic relaxation. Given that the Yangbi earthquake had a magnitude of Mw 6.1 and released limited energy [12], we can reasonably assume that the postseismic deformation was predominantly controlled by afterslip. We re-estimated the coseismic offsets and extracted the postseismic deformation through fitting the following logarithmic function:

$$S = C + P \times \log(1 + \frac{t - t_{eq}}{\tau}) \quad (5)$$

where S represents the LOS displacement time series, C denotes the coseismic offset, P is the amplitude of postseismic deformation, t represents the observation time, t_{eq} is the start time of postseismic deformation and τ is the postseismic relaxation time.

Out of the 21 postseismic descending orbit images, atmospheric conditions were rapidly changing as Yunnan approached summer, leading to reduced coherence of the interferometric pairs. Therefore, considering the image coherence, deformation level and function characteristics, we finally selected 14 images for fitting: 10 May, 22 May, 3 June, 15 June, 26 August, 1 October, 13 October, 25 October, 6 November, 18 November, 30 November, 2021, 5 January, 17 January and 29 January, all from 2022. These dates correspond to the observation dates marked by the blue triangles in the fitted curves in Figure 10.

We determined the constants C and P fixed by a grid search for the values of t_{eq} and τ with the least squares method. We prescribed t_{eq} to change from 1 min to 300 min in an increment of 1 min, and τ from 0.1 days to 100 days in increments of 0.1 days. For each time series, we fitted 300,000 curve models and determined the optimal fitting model with the smallest root mean square (RMS) of residuals. From 4991 uniform sampling points obtained using the grid sampling method, we selected 2191 points in total which exhibited convergence trends and minimal residuals. These selected points were nearly uniformly distributed on both sides of the coseismic deformation field (Figure 9).

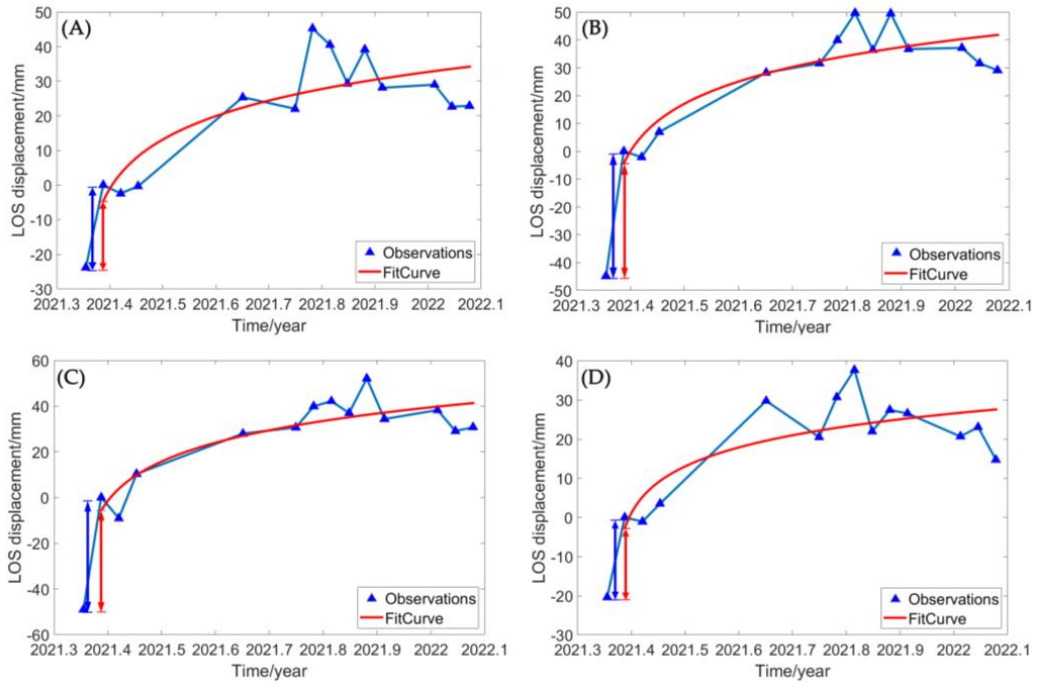


Figure 10. *Cont.*

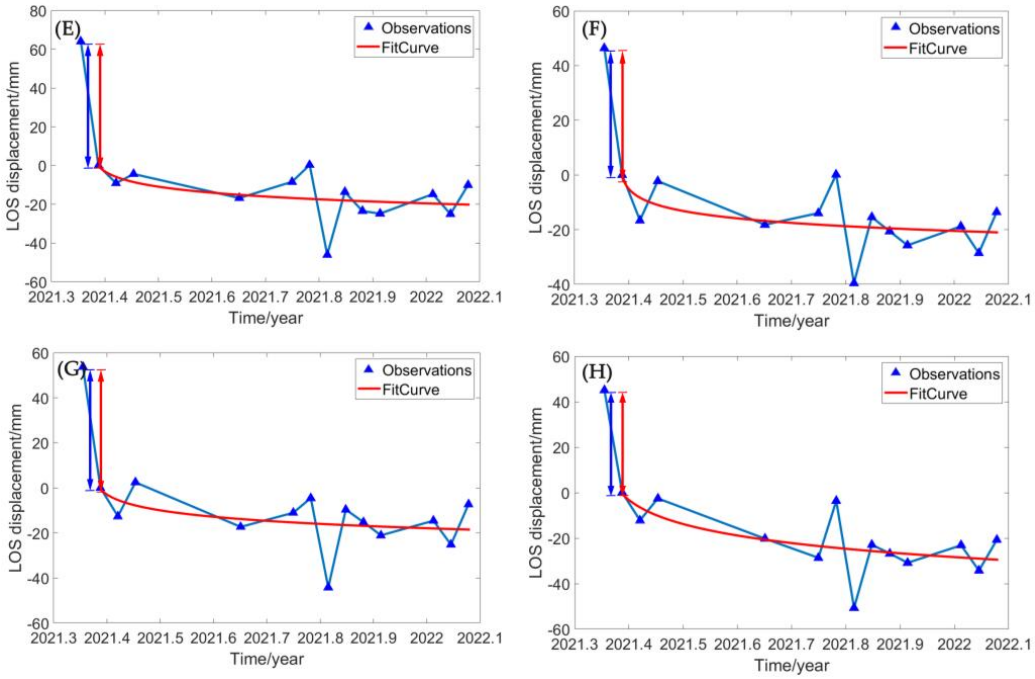


Figure 10. The postseismic fitting curves of the selected points (points **A**–**H**) in Figure 9. The blue arrows represent the coseismic observation values of the LOS directions at selected points, and the red arrows represent the coseismic values predicted by the postseismic fitting model at the selected points.

Figure 10 compares the raw time series and their refined fittings for eight points selected from the descending interferometric images (Figure 9). Points A, B, C and D are located in the areas exhibiting positive coseismic offsets, and Points E, F, G and H are located in the areas exhibiting negative coseismic offsets. The red curves represent the estimated logarithmic trends of the postseismic deformations. They show that the postseismic motion characteristics of most sampling points aligned with the coseismic direction, which somewhat enhanced the impact of the coseismic effect. The refined coseismic offsets were slightly smaller than those from the raw interferometric pairs. This suggests that the postseismic deformation process began before the acquisition time of the descending image on 22 May. As a result, coseismic offsets directly derived from the raw interferometric pairs between 10 May and 22 May 2021 included a certain fraction of postseismic deformation.

5.3. Refined Coseismic Slip and Afterslip Distributions

We further conducted two coseismic slip distribution inversions: one using the raw descending interferometric pairs directly and the refined model using the extracted coseismic jump C values for all selected points through nonlinear fitting. In order to retain the robustness of the comparison, both inversions were performed with the same smoothing factor on the same subfault model. Figure 11 shows that the refined fault slips were generally smaller than those obtained from the raw interferometric images. The overall slip was reduced, with the maximum slip decreasing from 0.35 m to 0.32 m and the moment magnitude decreasing from 6.11 to 6.05.

Figure 12 shows the temporal process of afterslip at seven snapshots that were taken on the 21st, the same date of the mainshock, from one month to half a year after the mainshock. It shows that the afterslip was concentrated at depths of 3 to 8 km and gradually increased over time. The maximum slip increased from 7 cm in June, with a moment magnitude of Mw5.6, to 20 cm in November, with a moment magnitude of Mw5.8, and then gradually stabilized. This indicates that the afterslip effect of the Yangbi earthquake persisted for nearly half a year.

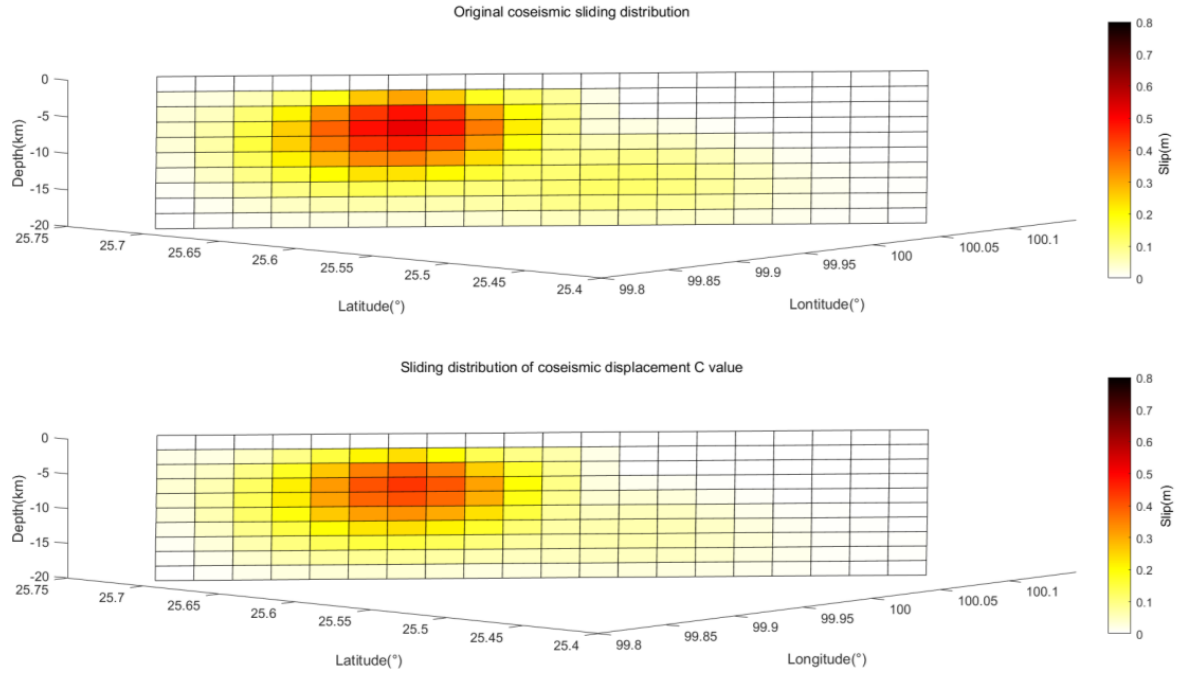


Figure 11. Comparison between slip inversions from (**top**) raw descending interferometric pairs and (**bottom**) refined coseismic offsets. Subfault dimension: 2 km × 2 km.

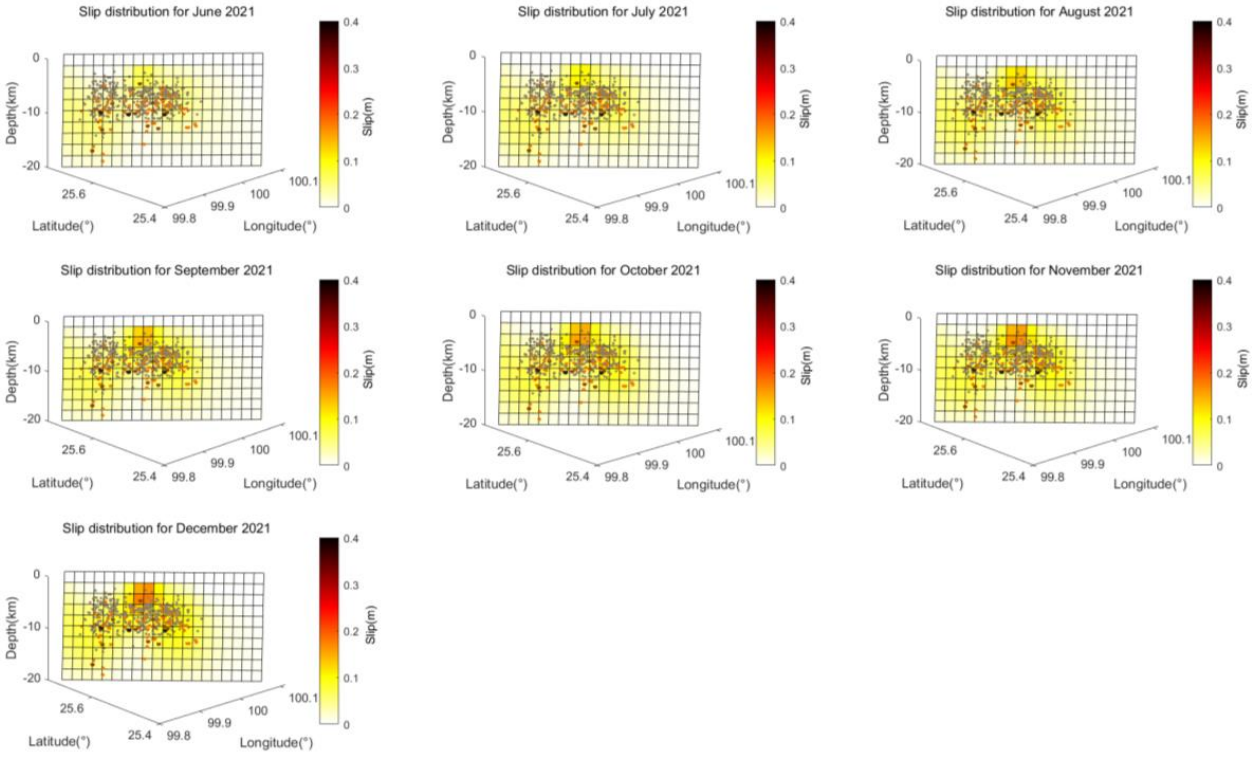


Figure 12. Characteristics of spatial distribution of fault slip due to postseismic afterslip.

6. Analysis and Discussion

In this paper, we first determined the fault geometry with a nonlinear least squares method by combining GNSS data and both ascending and descending InSAR data. Our inversions for the strike slip, dip slip, strike angle and dip angle (as shown in Table 5) were consistent with predictions from other institutions and researchers. The slip initiated at a depth of 2 km along the dip and extended down to 12 km, with the main slip spanning

from 4 km to 8 km downdip. More specifically, our fault slip distribution was consistent with the InSAR-based inversions using different methods [19,20]. The optimal rake angle identified in our model was −171°, indicating a pronounced right lateral strike-slip motion. This is in agreement with the results obtained by Chen et al. [29] using broadband regional seismic waveform data, underscoring the high consistency between our model and seismic waveform data. Our estimate of the dip angle was consistent with the dip angle of 80°, which was estimated with seismicity and combined InSAR and GNSS data (Zhang et al. [15], Wang et al. [17], Wang et al. [18]), whereas it was slightly flatter than that estimated with InSAR data (Lu et al. [19] (86°), Xu et al. [43] (89°), Zhang et al. [3] (86°)). This suggests that relying solely on InSAR data may lead to an overestimation of the fault dip angle, whereas incorporating GNSS data provides a better constraint on the dip angle. In addition, according to Lei et al. [53], the Ms5.6 seismic moment tensor of the Yangbi earthquake showed a significant non-double-couple component, suggesting that the earthquake may have been driven by deep high-pressure fluids. Therefore, modeling deformation based on subsurface faults under regional tectonic stress can only achieve a primary fit with some residual errors.

Meanwhile, we attempted to achieve fault geometric inversion using only single-view Sentinel images. Compared to the results from joint inversion, the inversion based on single-source data exhibited issues such as a shallower fault depth and narrower fault width. According to Wang et al. [18], the depth of the Yangbi fault derived from single-source SAR inversion ranged from 2 km to 9 km, which was slightly shallower than the depth of 3–13 km obtained by Zhang et al. [3] through the use of geodetic and teleseismic data. Lu et al. [19] indicated that single-source InSAR observations could increase the uncertainty of seismic slip and result in a shallower fault depth. However, the fault parameters obtained from the single-source ascending and descending track image inversion, such as the strike angle, dip angle, length and slip angle, were generally consistent with the results from joint data inversion. The fitting residuals for the ascending and descending tracks were 0.010 m and 0.011 m, respectively, slightly larger than the 0.009 m residuals from the joint inversion. Therefore, under limited conditions, the automated search based on single-source measurement data could still provide relatively reliable reference results.

The extraction of both the coseismic offsets and postseismic deformation may have been influenced by several factors. First, the Yangbi area was characterized by dense vegetation cover and variable topography, so the coherence of the images within the first three months after the earthquake was relatively poor, limiting the effectiveness of curve fitting. Both Figures 9 and 10 showed that the variations for certain months were particularly evident on 15 June and 25 October. The interferometric data on 15 June appeared to be generally lower, which might be attributed to the high vegetation cover around Yangbi and atmospheric factors that increased overall noise. Conversely, the October 25 image presented very distinct results, clearly delineating two separate zones. Such enhanced signals could be due to the favorable atmospheric conditions during image capture. Regardless of which cause, it is important to note that the presence of reasonable levels of noise did not impact the trend of postseismic deformation, allowing for accurate curve fitting in the analysis. Second, we found that the selection of sampling points significantly impacted the final inversion results. Selected reference points should be uniformly distributed on both sides of a coseismic deformation field and should include teleseismic information to constrain the deep slip of the fault. Third, due to the constraints of our study area, the Sentinel-1B images were not used in this time-series analysis. However, by precisely cropping the study area to the mainshock area and introducing Sentinel-1B images for time-series interferometric processing, along with integrating up-orbit images and GNSS data, the accuracy of coseismic signal constraints could be further improved.

7. Conclusions

In this study, we first determined fault geometry and inverted coseismic slip distribution by combining Sentinel-1A/B ascending and descending orbit observations with

GNSS data. Then, we refined coseismic slip distribution by eliminating the effects from the early postseismic deformation. Finally, we investigated the spatiotemporal evolution characteristics of afterslip. The results showed that the moment magnitude of the refined coseismic slip inferred from the postseismic deformation fitting using descending data was Mw 6.05, which is smaller than Mw 6.1, which was inferred from our joint inversion and previous studies. Predominantly located at depths of 4–6 km, afterslip extended over nearly six months and stabilized by November 2021, with a moment release equivalent to an Mw 5.8 earthquake. Most aftershocks are distributed beneath afterslip, indicating a spatially complementary pattern of distinct slip behaviors on a seismogenic fault. Our results suggested that utilizing InSAR data several days after the mainshock without correcting the postseismic effect would lead to an overestimation of coseismic slip. Besides offering a novel approach to extracting postseismic deformation from InSAR time series with large uncertainties, this study contributes to a better understanding of the seismic process of the Yangbi earthquake.

Supplementary Materials: The following supporting information can be downloaded at: https://www.mdpi.com/article/10.3390/rs16213996/s1, Figure S1: Gridded Sampling map of Ascending and Descending Orbits. (a) Gridded Sampling Map of ascending Orbits. (b) Gridded Sampling Map of descending Orbits.

Author Contributions: Conceptualization, Z.L. and K.Z.; methodology, K.Z.; software, Z.L.; validation, Z.L., K.Z. and S.L.; formal analysis, W.G.; investigation, Z.L.; writing—original draft preparation, Z.L. and K.Z.; writing—review and editing, Z.L. and K.Z.; supervision, W.G. All authors have read and agreed to the published version of the manuscript.

Funding: This research was funded by the National Key Research and Development Plan of China. (2019YFE0108900; 2018YFC1503304), National Natural Science Foundation of China (41974113) and National Nonprofit Fundamental Research Grant of China, Institute of Geology, China Earthquake Administration (IGCEA-20-02).

Data Availability Statement: The European Space Agency owns the copyright of the Sentinel-1 SAR data, and the Alaska Satellite Facility provided the downloading service through the https://search.asf.alaska.edu/#/, accessed on 25 July 2024). The Precise orbit information (AUX_POEORB) is publicly available via the European Space Agency (ESA, https://dataspace.copernicus.eu/, accessed on 25 July 2024). The GACOS atmospheric corrected data are available from the Generic Atmospheric Correction Online Service for InSAR, at http://www.gacos.net/, accessed on 25 July 2024.

Acknowledgments: We would like to express our gratitude to the four anonymous reviewers for their constructive comments and insightful suggestions, which have significantly improved our manuscript. We are deeply grateful to Chenglong Li, Yanchuan Li, Haoqing Liu and Chenglong Dai for their invaluable assistance in the InSAR data processing and constructive suggestions on the writing of this manuscript. Z.L. also sincerely thanks Zhaoyang Zhang for his valuable guidance and assistance in the drawing of the images for this paper. Some figures were prepared using tools from the public domain, Generic Mapping Tools (GMT) [54]. We give our great thanks to Rongjiang Wang for kindly sharing his SDM inversion package [55]. The interferometric processing of the images was based on the open-source ISCE platform, and the time series data processing was conducted using Mintpy provided by Zhang Yunjun. We again would like to express our gratitude for all the support.

Conflicts of Interest: The authors declare no conflicts of interest.

References

1. Long, F.; Qi, Y.; Yi, G.; Wu, W.; Wang, G.; Zhao, X. Relocation of the M_S6.4 Yangbi earthquake sequence on May 21, 2021 in Yunnan Province and its seismogenic structure analysis. *Chin. J. Geophys.* **2021**, *64*, 2631–2646.
2. Su, J.; Liu, M.; Zhang, Y.; Wang, W.; Li, H.; Yang, J.; Li, X.; Zhang, M. High resolution earthquake catalog building for the 21 May 2021 Yangbi, Yunnan, M_S6.4 earthquake sequence using deep-learning phase picker. *Chin. J. Geophys.* **2021**, *64*, 2647–2656.
3. Zhang, B.; Xu, G.; Lu, Z.; He, Y.; Peng, M.; Feng, X. Coseismic deformation mechanisms of the 2021 M_S6.4 Yangbi earthquake, Yunnan Province, using InSAR observations. *Remote Sens.* **2021**, *13*, 3961. [CrossRef]
4. Yang, J.; Wen, Y.; Xu, C. The 21 May 2021 M_S6.4 Yangbi (Yunnan) earthquake: A shallow strike-slip event rupturing in blind fault. *Chin. J. Geophys.* **2021**, *64*, 3101–3110. (In Chinese)

5. Yang, Z.; Liu, J.; Zhang, X.; Deng, W.; Du, G.; Wu, X. A preliminary report of the Yangbi, Yunnan, M_S6.4 earthquake of May 21, 2021. *Earth Planet. Phys.* **2021**, *5*, 362–364. [CrossRef]
6. Yan, K.; Wang, W.; Peng, F.; Wang, Q.; Kou, H.; Yuan, A. The seismogenic structures and migration characteristics of the 2021 Yangbi M_S6.4 Earthquake sequence in Yunnan, China. *Sci. China Earth Sci.* **2022**, *65*, 1522–1537. [CrossRef]
7. Zhao, D.; Qu, C.; Shan, X.; Bürgmann, R.; Gong, W.; Tung, H.; Zhang, G.; Song, X.; Qiao, X. Multifault complex rupture and afterslip associated with the 2018 M_W6.4 Hualien earthquake in northeastern Taiwan. *Geophys. J. Int.* **2021**, *224*, 416–434. [CrossRef]
8. Zhou, Y.; Ren, C.; Ghosh, A.; Meng, H.; Fang, L.; Yue, H.; Zhou, S.; Su, Y. Seismological Characterization of the 2021 Yangbi Foreshock-Mainshock Sequence, Yunnan, China: More than a Triggered Cascade. *J. Geophys. Res.* **2022**, *127*, e2022JB024534. [CrossRef]
9. Ye, T.; Chen, X.; Huang, Q.; Cui, T. Three-dimensional electrical resistivity structure in focal area of the 2021 Yangbi M_S6.4 Earthquake and its implication for the seismogenic mechanism. *Chin. J. Geophys.* **2021**, *64*, 2267–2277.
10. Li, D.; Ding, Z.; Wu, P.; Liu, S.; Deng, F.; Zhang, X.; Zhao, H. The characteristics of crustal structure and seismogenic background of Yangbi M_S6.4 earthquake on May 21, 2021 in Yunnan Province, China. *Chin. J. Geophys.* **2021**, *64*, 3083–3100.
11. Sun, Q.; Guo, Z.; Pei, S.; Fu, Y.; Chen, Y. Fluids triggered the 2021 M_w6.1 Yangbi earthquake at an unmapped fault: Implications for the tectonics at the northern end of the red river fault. *Seismol. Res. Lett.* **2022**, *93*, 666–679. [CrossRef]
12. Gong, W.; Ye, L.; Qiu, Y.; Lay, T.; Kanamori, H. Rupture directivity of the 2021 M_w6.0 Yangbi, Yunnan earthquake. *J. Geophys. Res.* **2022**, *127*, e2022JB024321. [CrossRef]
13. Zhu, G.; Yang, H.; Tan, Y.; Jin, M.; Li, X.; Yang, W. The cascading foreshock sequence of the M_S6.4 Yangbi earthquake in Yunnan, China. *Earth Planet. Sci. Lett.* **2022**, *591*, 117594. [CrossRef]
14. Liang, S.; Guo, R.; Yang, H.; Tang, X.; Xu, X.; Gan, W. Rupture imaging of the 2021 M_S6.4 Yangbi, China, earthquake: Implications for the diffuse deformation in the northern region of the Red River fault. *Tectonophysics* **2023**, *862*, 229932. [CrossRef]
15. Zhang, K.; Gan, W.; Liang, S.; Xiao, G.; Dai, C.; Wang, Y.; Li, Z.; Zhang, L.; Ma, G. Coseismic displacement and slip distribution of the 2021 May 21, M_S6.4, Yangbi Earthquake derived from GNSS observations. *Chin. J. Geophys.* **2021**, *64*, 2253–2266.
16. Li, C.; Shan, X.; Zhang, G.; Zhao, C.; Gong, W.; Zhang, Y. Slip kinematics of the 2021 Yangbi earthquake: Fore-Main-Aftershock sequence rupture along an unknown secondary fault of the Weixi–Qiaohou fault. *Seismol. Res. lett.* **2022**, *93*, 1400–1412. [CrossRef]
17. Wang, S.; Liu, Y.; Shan, X.; Qu, C.; Zhang, G.; Xie, Z.; Zhao, D.; Fan, X.; Hua, J.; Liang, S. Coseismic surface deformation and slip models of the 2021 M_S6.4 Yangbi (Yunnan, China) earthquake. *Seismol. Geol.* **2021**, *43*, 692–705.
18. Wang, Y.; Chen, K.; Shi, Y.; Zhang, X.; Chen, S.; Li, P.; Lu, D. Source model and simulated strong ground motion of the 2021 Yangbi, China shallow earthquake constrained by InSAR observations. *Remote Sens.* **2021**, *13*, 4138. [CrossRef]
19. Lu, H.; Feng, G.; He, L.; Liu, J.; Gao, H.; Wang, Y.; Wu, X.; Wang, Y.; An, Q.; Zhao, Y. An Improved Source Model of the 2021 M_w6.1 Yangbi Earthquake (Southwest China) Based on InSAR and BOI Datasets. *Remote Sens.* **2022**, *14*, 4804. [CrossRef]
20. Li, X.; Wang, C.; Zhu, C.; Wang, S.; Li, W.; Wang, L.; Zhu, W. Coseismic deformation field extraction and fault slip inversion of the 2021 Yangbi M_w6.1 earthquake, Yunnan Province, based on time-Series InSAR. *Remote Sens.* **2022**, *14*, 1017. [CrossRef]
21. Tian, J.; Gao, Y.; Luo, Y. Deep seismogenic tectonics of Yangbi M_S6.4 on 21 May 2021 in the SE margin of the Tibetan plateau from earthquake sequence relocation, stress field and seismic anisotropy. *Tectonophysics* **2023**, *851*, 229768. [CrossRef]
22. Peng, Z.; Gomberg, J. An integrated perspective of the continuum between earthquakes and slow-slip phenomena. *Nat. Geosci.* **2010**, *3*, 599–607. [CrossRef]
23. Tobita, M. Combined logarithmic and exponential function model for fitting postseismic GNSS time series after 2011 Tohoku-Oki earthquake. *Earth Planets Space* **2016**, *68*, 41. [CrossRef]
24. Langbein, J.; Murray, J.; Snyder, H. Coseismic and initial postseismic deformation from the 2004 Parkfield, California, earthquake, observed by Global Positioning System, electronic distance meter, creepmeters, and borehole strainmeters. *Bull. Seismol. Soc. Am.* **2006**, *96*, S304–S320. [CrossRef]
25. Ragon, T.; Sladen, A.; Bletery, Q.; Vergnolle, M.; Cavalié, O.; Avallone, A.; Balestra, J.; Delouis, B. Joint inversion of coseismic and early afterslip to optimize the information content in geodetic data: Application to the 2009 M_w6.3 L'Aquila earthquake, Central Italy. *J. Geophys. Res.* **2019**, *124*, 10522–10543. [CrossRef]
26. Bruhat, L.; Barbot, S.; Avouac, J.-P. Evidence for postseismic deformation of the lower crust following the 2004 M_w6. 0 Parkfield earthquake. *J. Geophys. Res. Solid Earth* **2011**, *116*, B08401. [CrossRef]
27. Johanson, I.; Fielding, E.; Rolandone, F.; Bürgmann, R. Coseismic and afterslip of the 2004 Parkfield earthquake from space-geodetic data. *Bull. Seismol. Soc. Am.* **2006**, *96*, S269–S282. [CrossRef]
28. Klein, E.; Bock, Y.; Xu, X.; Sandwell, D.T.; Golriz, D.; Fang, P.; Su, L. Transient deformation in California from two decades of GPS displacements: Implications for a three-dimensional kinematic reference frame. *J. Geophys. Res.* **2019**, *124*, 12189–12223. [CrossRef]
29. Chen, J.; Hao, J.; Wang, Z.; Xu, T. The 21 May 2021 M_w6.1 Yangbi earthquake—A unilateral rupture event with conjugately distributed aftershocks. *Seismol. Res. Lett.* **2022**, *93*, 1382–1399. [CrossRef]
30. Liu, X.; Xu, W.; He, Z.; Fang, L.; Chen, Z. Aseismic slip and cascade triggering process of foreshocks leading to the 2021 M_w6.1 Yangbi earthquake. *Seismol. Res. Lett.* **2022**, *93*, 1413–1428. [CrossRef]
31. Wei, J.; Li, Z.; Hu, J.; Feng, G.; Duan, M. Anisotropy of atmospheric delay in InSAR and its effect on InSAR atmospheric correction. *J. Geod.* **2018**, *93*, 241–265. [CrossRef]

32. Deng, Q.; Zhang, P.; Ran, Y.; Yang, X.; Min, W.; Chu, Q. Basic characteristics of active tectonics of China. *Sci. China Ser. D Earth Sci.* **2003**, *10*, 66–73. (In Chinese) [CrossRef]
33. Liu, P.; Ren, T. Arias intensity attenuation relationship in Sichuan–Yunnan region, China. *Bull. Earthq. Eng.* **2022**, *20*, 6377–6406. [CrossRef]
34. Tang, P.; Chang, Z. Activity of the Weishan Basin Segment of the Weixi-Qiaohou Fault. *Geol. Rev.* **2013**, *59*, 108–109. (In Chinese)
35. Li, C.; Zhang, J.; Wang, W.; Sun, K.; Shan, X. The seismogenic fault of the 2021 Yunnan Yangbi M_S6.4 Earthquake. *Seismol. Egol.* **2021**, *43*, 706–721. (In Chinese)
36. Rosen, P.; Gurrola, E.; Sacco, G.F.; Zebker, H. The InSAR scientific computing environment. In Proceedings of the EUSAR 2012 9th European Conference on Synthetic Aperture Radar, Nürnberg, Germany, 23–26 April 2012; Volume 23, pp. 730–733.
37. Izumi, Y.; Takeuchi, W.; Widodo, J.; Sulaiman, A.; Awaluddin, A.; Aditiya, A.; Razi, P.; Anggono, T.; Sumantyo, J.T.S. Temporal Subset SBAS InSAR Approach for Tropical Peatland Surface Deformation Monitoring Using Sentinel-1 Data. *Remote Sens.* **2022**, *14*, 5825. [CrossRef]
38. Farr, T.G.; Rosen, P.A.; Caro, E.; Crippen, R.; Duren, R.; Hensley, S.; Kobrick, M.; Paller, M.; Rodriguez, E.; Roth, L. The shuttle radar topography mission. *Rev. Geophys.* **2007**, *45*, RG2004. [CrossRef]
39. Goldstein, R.M.; Werner, C.L. Radar interferogram filtering for geophysical applications. *Geophys. Res. Lett.* **1998**, *25*, 4035–4038. [CrossRef]
40. Yu, C.; Li, Z.; Penna, N.T.; Crippa, P. Generic atmospheric correction model for interferometric synthetic aperture radar observations. *J. Geophys. Res. Solid Earth* **2018**, *123*, 9202–9222. [CrossRef]
41. Li, Z.; Xu, W.; Feng, G.; Hu, J.; Wang, C.; Ding, X.; Zhu, J. Correcting atmospheric effects on InSAR with MERIS water vapour data and elevation-dependent interpolation model. *Geophys. J. Int.* **2012**, *189*, 898–910. [CrossRef]
42. Werner, C.; Wegmüller, U.; Strozzi, T.; Wiesmann, A. Processing strategies for phase unwrapping for INSAR applications. In Proceedings of the European Conference on Synthetic Aperture Radar (EUSAR 2002), Cologne, Germany, 4–6 June 2002; pp. 353–356.
43. Xu, X.; Ji, L.; Zhu, L.; Wang, G.; Zhang, W.; Li, N. The coseismic deformation characteristics and seismogenic structure of the yangbi M_S6.4 earthquake. *Seismol. Geol.* **2021**, *43*, 771–789.
44. Wang, C.; Ding, X.; Shan, X.; Zhang, L.; Jiang, M. Slip distribution of the 2011 Tohoku earthquake derived from joint inversion of GPS, InSAR and seafloor GPS/acoustic measurements. *J. Asian Earth Sci.* **2012**, *57*, 128–136. [CrossRef]
45. Okada, Y. Surface deformation due to shear andtensile faults in a half-space. Bull. *Seismol. Soc. Am.* **1985**, *75*, 1135–1154. [CrossRef]
46. Marquardt, D.W. An algorithm for least-squares estimation of nonlinear parameters. *J. Soc. Ind. Appl. Math.* **1963**, *11*, 431–441. [CrossRef]
47. Luo, X.; Sun, J.; Shen, Z.; Yo, F. Coseismic Slip Distribution of 2010 Darfield M_w7.1 Earthquake Derived from InSAR Measurements. *Chin. J. Geophys.* **2013**, *56*, 117–128.
48. Feng, G.; Ding, X.; Li, Z.; Mi, J.; Zhang, L.; Omura, M. Calibration of an InSAR-derived coseimic deformation map associated with the 2011 Mw-9.0 Tohoku-Oki earthquake. *IEEE Geosic. Remote Sens. Lett.* **2012**, *9*, 302–306. [CrossRef]
49. Yang, T.; Li, B.; Fang, L.; Su, Y.; Zhong, Y.; Yang, J.; Qin, M.; Xu, Y. Relocation of the Foreshocks and Aftershocks of the 2021 M_S6.4 Yangbi Earthquake Sequence, Yunnan, China. *J. Earth Sci.* **2022**, *33*, 892–900. [CrossRef]
50. Chang, Z.; Zang, Y.; Chang, H. New discovery of holocene activity along the Weixi-Qiaohou fault in southeastern margin of the Tibetan plateau and its neotectonic significance. *Acta Geol. Sin.* **2018**, *92*, 2464–2465.
51. Zhang, Y.; Heresh, F.; Falk, A. Small baseline InSAR time series analysis: Unwrapping error correction and noise reduction. *Comput. Geosci.* **2019**, *133*, 104331.
52. Li, Z.; Muller, J.-P.; Cross, P.; Fielding, E. Interferometric syntheric aperture radar (InSAR) atmospheric correction GPS, Moderate Resolution Imaging Spectroradiometer (MODIS), and InSAR integration. *J. Geophys. Res. Space Phys.* **2005**, *110*, B03410.
53. Lei, X.; Wang, Z.; Ma, S. A preliminary study on the characteristics and mechanism of the May 2021 M_s6.4 Yang Bi earthquake sequence, Yunnan, China. *Acta Seismol. Sin.* **2021**, *43*, 261–286.
54. Wessel, P.; Smith, W. New improved version of generic mapping tools released. *EOS Trans. Am. Geophys. Union* **1998**, *79*, 579. [CrossRef]
55. Wang, R.; Diao, F.; Hoechner, A. SDM—A geodetic inversion code incorporating with layered crust structure and curved fault geometry. In Proceedings of the European Geosciences Union Conference, Vienna, Austria, 7–12 April 2013; EGU General Assembly: Vienna, Austria, 2013.

Disclaimer/Publisher's Note: The statements, opinions and data contained in all publications are solely those of the individual author(s) and contributor(s) and not of MDPI and/or the editor(s). MDPI and/or the editor(s) disclaim responsibility for any injury to people or property resulting from any ideas, methods, instructions or products referred to in the content.